Measuring water level in rivers and lakes from lightweight Unmanned Aerial Vehicles

Bandini, Filippo; Jakobsen, Jakob; Olesen, Daniel Haugård; Reyna-Gutiérrez, José Antonio; Bauer-Gottwein, Peter

Published in:
Journal of Hydrology

Link to article, DOI:
10.1016/j.jhydrol.2017.02.038

Publication date:
2017

Document Version
Peer reviewed version

Journal of Hydrology and in press.

Measuring water level in rivers and lakes from lightweight Unmanned Aerial Vehicles

Filippo Bandini[*1], Jakob Jakobsen[2], Daniel Olesen[2], Jose Antonio Reyna-Gutierrez[1], Peter Bauer-Gottwein[1]

*Corresponding author: fban@env.dtu.dk

[1]*Department of Environmental Engineering, Technical University of Denmark, 2800, Lyngby, Denmark*

[2]*National Space Institute, Technical University of Denmark, 2800, Lyngby, Denmark*

Highlights

- Water level of rivers and lakes can be measured by Unmanned Aerial Vehicles.
- Unmanned Aerial Vehicles ensure high accuracy and spatial resolution.
- The measuring system consists of a ranging sensor and a GNSS receiver.
- Among the ranging sensors, the radar has the highest accuracy and longest range.
- The camera-laser sensor is preferred for narrow field of view to water surface.

Abstract

The assessment of hydrologic dynamics in rivers, lakes, reservoirs and wetlands requires measurements of water level, its temporal and spatial derivatives, and the extent and dynamics of open water surfaces. Motivated by the declining number of ground-based measurement stations, research efforts have been devoted to the retrieval of these hydraulic properties from spaceborne platforms in the past few decades. However, due to coarse spatial and temporal resolutions, spaceborne missions have several limitations when assessing the water level of terrestrial surface water bodies and determining complex water dynamics. Unmanned Aerial Vehicles (UAVs) can fill the gap between spaceborne and ground-based observations, and provide high spatial resolution and dense temporal coverage data, in quick turn-around time, using flexible payload design. This study focused on categorizing and testing sensors, which comply with the weight constraint of small UAVs (around 1.5 kg), capable of measuring the range to water surface. Subtracting the measured range from the vertical position retrieved by the onboard Global Navigation Satellite System (GNSS) receiver, we can determine the water level (orthometric height). Three different ranging payloads, which consisted of a radar, a sonar and an in-house developed camera-based laser distance sensor (CLDS), have been evaluated in terms of accuracy, precision, maximum ranging distance and beam divergence. After numerous flights, the relative accuracy of the overall system was estimated. A ranging accuracy better than 0.5 % of the range and a maximum ranging distance of 60 m were achieved with the radar. The CLDS showed the lowest beam divergence, which is required to avoid contamination of the signal from interfering surroundings for narrow fields of view. With the GNSS system delivering a relative vertical accuracy better than 3-5 cm, water level can be retrieved with an overall accuracy better than 5-7 cm.

Keywords: UAV; water level; radar; sonar; laser; GPS;

1. Introduction

Extreme hydro-climatic events such as droughts, floods and heavy precipitation have increased the awareness that knowledge of spatial and temporal variation of open water surfaces is important (Alsdorf et al., 2007). In order to achieve a better quantitative understanding of hydrologic processes and to increase sharpness and reliability of hydrologic predictions, observations of hydrological variables, such as surface water area, water level (h), its slope ($\partial h/\partial x$) and its temporal change ($\partial h/\partial t$) are required. However, ground-based measurements of terrestrial water bodies are limited to networks of measuring stations. In-situ stations provide point observations that are often spaced too far apart to capture spatial patterns. Often, in-situ observation technology fails during extreme events. Furthermore, globally, the availability of in-situ hydrologic observation stations has been declining in the recent past (Lawford et al., 2013). Hence, remote sensing datasets have become increasingly popular in hydrology. Remote sensing techniques are presently unable to observe river discharge directly, however spatial and temporal variation of water level has been routinely observed using spaceborne or airborne platforms. Although most satellite altimetry missions were not designed primarily for monitoring continental waters, water levels of continental water surfaces retrieved by Seasat, TOPEX/Poseidon, Jason-1 and 2, GFO, ERS 1 and 2, ENVISAT have a measurement accuracy that is well understood and generally on the order of a few tens of centimeters (Calmant et al., 2008). This accuracy can be improved for larger lakes and rivers by averaging over large water surfaces (Birkett, 1998; Birkett et al., 2002; Frappart et al., 2006). The satellite CryoSat-2 carries a Synthetic Aperture Interferometric Radar Altimeter (SIRAL) which is a new generation radar altimeter (Wingham et al., 2006) with a spatial resolution of around 300 m (Villadsen et al.,

2015). When operating in SARIn mode, a correction of the cross-track slope can be performed and waveform analysis allows separation between water and surrounding topography (Kleinherenbrink et al., 2014) resulting in an accuracy of the retrieved water level of just a few decimeters (Kleinherenbrink et al., 2015). Spaceborne LIDARs such as the Geoscience Laser Altimeter System (GLAS) have been shown to provide water level measurements with higher accuracy than radar altimeters such as TOPEX/Poseidon (Zhang and Xie, 2010). Still, GLAS has a ground footprint that is around 65 m (Schutz et al., 2005) and retrieves observations at irregular temporal intervals. Therefore, the main limitations of conventional satellite radar and laser altimetry are low spatial resolution, local coverage (for short repeat orbit missions) and low temporal resolution (for long repeat missions such as CryoSat). In order to overcome these limitations, the forthcoming Surface Water and Ocean Topography (SWOT) satellite mission will build on the heritage of the imaging interferometric radars such as the Shuttle Radar Topography Mission (SRTM) (Kiel et al., 2006; LeFavour and Alsdorf, 2005; Rodriguez et al., 2006). However, spaceborne sensors will always face problems of: i) large ground footprints, which result in relatively low spatial resolution; ii) fixed orbit configurations, which may be inappropriate for high-resolution coverage of local water bodies; iii) coarse temporal resolution and/or the non-regular revisit intervals. These limitations restrict their ability to measure the temporal and spatial variation of the water level with the accuracy needed for determining the hydraulics of complex rivers and flood waves.

Airborne LIDAR techniques have the advantages of better tracking of terrestrial water bodies, improved spatial resolution, clear segmentation between land and water surfaces and a higher accuracy (Schumann et al., 2008). However, airborne LIDAR surveys are expensive and their success depends on surveying conditions (e.g. topography and geometry, vegetation cover, size

of the water body). For this reason, digital elevation models and digital surface models retrieved by airborne LIDAR are not universally available and are normally not retrieved during periods of hydrological interest such as flood events.

UAVs (Unmanned Aerial Vehicles) and in particular micro-UAVs (payload less than 1.5-2 kg), represent the latest frontier in land and water monitoring because of low-altitude flight, low cost and flexible payload design (Anderson and Gaston, 2013). In recent years, miniaturized components (GNSS receivers, inertial measurement units, autopilots) have advanced (Watts et al., 2012), and UAVs have been used also for a wide range of hydrological applications such as fluvial monitoring; river bathymetry and photogrammetric DEM generation using very high resolution (VHR) imagery (Lejot et al., 2007); water velocity measurements using large-scale particle image velocimetry (LSPIV) (Detert and Weitbrecht, 2015; Tauro et al., 2016, 2015). Moreover, UAVs have attracted great interest for monitoring of environmental disasters and floods (Luo et al., 2015). UAVs are low-cost platforms that have unique capabilities to access hostile or inaccessible environments that need to be urgently monitored. Moreover, they ensure tracking of water surfaces better than satellite technology. However, for LIDAR and SAR systems, the tradeoff between performance, cost and size/weight is still a challenge to be solved before their application in UAV remote sensing (Colomina and Molina, 2014).

In this paper, we demonstrate the possibility to acquire measurements of water level by a ranging system that includes a ranging sensor (radar, CLDS or sonar) and a GNSS receiver. The ranging technology described in this paper provides water level measurements with higher accuracy than spaceborne or airborne altimetry. Moreover, it ensures a spatial resolution ideal for measuring the two dimensional spatial variability of small rivers and their interaction with floodplains (Lee et al., 2011). Lastly, the newly developed CLDS can acquire ranges to water surfaces when only

narrow fields of view are available. The CLDS is specifically developed for applications in vegetated environments or inside sinkholes in karst environments.

2. Materials and Methods

2.1. General concept

To acquire accurate water level (height above mean sea level) of open water surfaces, the UAV must be equipped with: i) accurate lightweight sensors for measuring the range to water surface ii) a high accuracy dual frequency GNSS receiver and antenna. Installation of an in-situ dual frequency GNSS master station is needed for differential corrections. The general concept is illustrated in Fig. 1.

Fig. 1.

The ellipsoidal height of the water surface is measured by subtracting the range measured by a ranging sensor from the vertical position retrieved by the onboard GNSS receiver. Afterwards the orthometric height can be retrieved from the ellipsoidal height if the geoid height is known (Featherstone, 2001). For the purpose of this work, a hexacopter has been assembled from TAROT-RC components and has been equipped with DJI Naza-M2 flight controller. The hexacopter is able to fly at least 12 minutes carrying a payload of at most 2 kg. The choice of the ranging sensors was constrained by: i) maximum weight of the payload, ii) a reasonable price necessary for flexible operations, iii) sensor interfaces that allow time synchronization with the GNSS receiver through a microprocessor. The selected ranging sensors included two off-the-

shelf sensors (a radar, a sonar) and the in-house developed CLDS. The total cost of the platform is ca. 7000 euros. This cost includes the drone, the onboard GNSS system, the inertial measurement unit (IMU), the three tested sensors and the microprocessor unit.

Fig. *2* shows the arrangement of the drone payload.

Fig. 2

2.1.1. Radar ranger

The radar is the ARS 30X model developed by Continental as anti-collision system for the automotive industry (market price: 3200 EUR). It weighs around 350 g and consists of a 77 GHz radar sensor with a mechanical scanning antenna. It measures the range to targets using FMCW (Frequency Modulated Continuous Wave) with a sampling frequency of 15 measurements per second. It provides up to 32 targets in near range and up to 64 targets in far range with a resolution of 0.10 m. Each individual target angle is provided with a resolution of 0.1˚.

2.1.2. Sonar ranger

The sonar is the MB7386 model from MaxBotix (market price: 150 EUR). It weighs around 50g and consists of a 42 kHz ultrasonic sensor (6 Hz reading rate) with internal temperature

compensation, noise tolerance and clutter rejection. Its maximum ranging capability is up to 10 m.

2.1.3. Camera-based laser distance sensor (CLDS)

This ranging sensor is a laser camera-based solution recently developed at Technical University of Denmark (Reyna Gutierrez, 2013). It weighs around 350 g. It was inspired by the measuring procedure proposed by Danko (2004). The range distance to the target is estimated by measuring the angle at which laser light enters the camera. The original methodology is expanded in this work to include corrections for tilting and rotation angles of the aircraft. An efficient automatic algorithm for identifying the laser dots on the water surface was developed. Our prototype consists of two laser pointers (100 mW laser diodes) and a complementary metal–oxide–semiconductor (CMOS) camera. The camera resolution is 20.2 megapixels. The camera is triggered by the on-board single board computer (SBC) with an image rate of 1 frame every 2.5 seconds. The total manufacturing cost of this CLDS system is around 800 EUR. The current design of the distance-meter includes a digital camera mounted at the center between the two laser pointers. Fig. *3* shows the geometrical configuration of the camera. Range to water surface is measured by illuminating the water surface with the laser pointers and taking a picture of the illuminated water surface. When light emitted by laser pointers hits the water surface, bright dots are formed at the interface between water and air. Due to scattering processes (in particular Rayleigh and Mie scattering), some portion of the radiation is reflected in the direction of the camera and an estimation of the range to water surface is possible.

Fig. 3.

The angle α is a design parameter. The CLDS was built with α =90̊ to simplify the measuring concept and the derivation of the formulas. The CLDS shown in Fig. *3* is exactly symmetrical. Indeed, only one laser would be sufficient to acquire the range to the surface; nevertheless, two laser pointers improve error assessment and system accuracy.

The value of the measured range Hm can be computed by measuring the angle θ′ at which light enters the camera, i.e. from equation (1).

$$Hm = \frac{A}{\tan\theta'} \tag{1}$$

Alternatively, the measured range Hm can be obtained through equation (2)

$$Hm = \frac{A \cdot f}{ImD} \tag{2}$$

Where ImD (Image distance) is the distance between the center of the image and the recorded light source. A calibration procedure is needed to convert from the number of pixels from the center of the image (PFC) to ImD as shown in equation (3)

$$ImD = PFC \cdot d_{pp1} + d_0 \tag{3}$$

Where d_{pp1} and d_0 are the coefficients of the first-order polynomial producing the best least-squares fit to the data. Equations (2) and (3) can be applied only when the focal length (f) of the camera is exactly and the focus is constantly set to infinity. Otherwise, the calibration procedure needs to estimate the angle θ′ directly from the number of pixels (PFC) as shown in equation (4).

$$\theta' = \mathrm{P}FC \cdot r_{pp1} + r_0 \tag{4}$$

Where r_{pp1} and r_0 are the coefficients of the first-order polynomial producing the best least-squares fit to the data. The calibration procedure, which has to be performed to estimate the r_{pp1} and r_0 coefficients, is presented in the appendix. The calibration procedure allows estimation of the angle θ' by measuring PFC, without having to consider the linear or nonlinear intrinsic camera parameters, such as focal length and lens distortion.

Onboard the UAV, tilting and rotation cause a displacement of the light sources from their equilibrium position. The changes in the geometrical relationships generate an error in the estimation of the true range distance (hereafter defined as Ht) between the sensor of the camera and the water surface. Tilting is the angle between the plane on which the camera and laser are located, i.e. the axis of the CLDS, and the horizontal plane (angle β as shown in Fig. *4*). Rotation occurs between the vertical line and the optical axis of the camera (angle δ as shown in Fig. 5).

Fig. 4

Fig. 5

If tilting pushes the light source below the axis of the distance meter, formula (5) can be used to obtain the true range (Ht) between the camera and the water surface:

$$\mathrm{Ht} = [\ (Hm + A \cdot \tan\beta) \cos\beta\ ] \cdot \cos\delta \quad (5)$$

Conversely, if the tilting pushes the light source above the axis of the CLDS, formula (6) can be used:

$$\mathrm{Ht} = [\ (Hm - A \cdot \tan\beta) \cos\beta\ ] \cdot \cos\delta \quad (6)$$

If pitch and roll angles are retrieved on board the UAV, the measured range can be corrected according to equation (5) and (6) (Reyna Gutierrez, 2013). If the angles are not retrieved on board, the resulting error on the range can be estimated as shown in Fig. 6. Numerous tests have been conducted in order to determine the best configuration of the CLDS in terms of: i) arm length A, ii) wavelengths of the two laser pointers, iii) optimal camera configuration parameters such as optical zoom and resolution.

The arm length choice affects the measuring range function, as shown in Fig. 7.

Fig. 6 **Fig.** 7

Fig. 7 shows that the resolution of the measurements depends on the derivative of the range function. Hence, a longer arm will result in higher resolution, especially for longer ranges. Indeed, in Fig. 7, the smoothest curve is for an arm length of 0.6 m. However, the payload size of small UAVs is limited and thus a 30 cm arm was chosen for our tests. The wavelengths of the two laser pointers were chosen as 450 nm and 531 nm, because reflectivity of water is relatively

high at these wavelengths as a consequence of the optical proprieties of water as described in Hale and Querry (1973).

When the laser light hits the water surface, a bright dot is formed at the point of contact. However, additional bright spots might be visible due to reflection from the riverbed and due to additional scattering processes caused by water waves. To identify the two dots formed by laser reflection, an automatic identification algorithm was developed consisting of the following computational steps: i) the RGB image is converted to Hue, Saturation and Value (HSV) image. Quasi-circular shapes in the image are found through circular Hough transform (Yuen et al., 1990). In case there are multiple circles in the image, the two circles (one generated by the left laser and one by the right laser) with the highest mean Value (V) are considered to be the contact spots. Thereafter, ii) the brightest pixel (pixel with the highest Value) is identified inside each of the two circles (laser dots). The brightest pixel typically lies in the center of the laser dot in case of normal light incidence. Lastly, iii) the distance (PFC) between the center of the image and the two identified brightest pixels is computed. Post-processing of the images is performed after the flight and takes around 30 seconds per image.

2.1.4. GNSS system

The differential GNSS system consists of two NovAtel receivers: one used as master station (flexpack6) and one as rover (OEM628 board). A NovAtel GPS-703-GGG pinwheel triple frequency and GLONASS antenna is used as base station and an antcom (3G0XX16A4-XT-1-4-Cert) dual frequency GPS and GLONASS flight antenna is used as rover station on the UAV. Raw pseudoranges and carrier phase measurements are stored at 5 Hz. The position solution is post-processed using Leica Geomatic Office v 8.1 in kinematic mode. In post-processed mode, a Kalman filter can be applied both in forward and backward direction for best position

performance. The length of the GPS baseline affects the vertical and horizontal accuracy of the drone position. Position error is expected to increase by 1-3 ppm (1-3 mm additional error per km of baseline).

2.1.5. Payload controller

Data acquired by the different sensors are saved on the SBC (BeagleBone Black) and a time synchronization of the different sensors can be performed. Synchronization between the position retrieved by the GNSS system and the range retrieved by the sensors is essential for accurate water level observations, as described in Appendix B.

2.2. Testing of the sensors

To test the accuracy of the system, both static (ground-based) and dynamic (airborne) tests were performed. First, several tests were conducted from bridges of different heights over free-flowing rivers in order to test accuracy, precision and maximum ranging capability. Beam divergence was tested by acquiring measurements inside a water well of small diameter. After the ground-based tests, numerous flight tests were conducted over a lake. Because the water level in the lake can be assumed to be uniform in space, these flights allowed determination of the accuracy of the full system, which consists of the GNSS receiver and the ranging sensors. Appendix B reports the experimental settings of both static and airborne tests.

2.2.1. Ground-based evaluation

Accuracy of the ranging sensors was estimated using as reference a water level dip meter, which has an accuracy better than 0.3% of the range. When tested in static mode, sensors acquired measurements for 30 seconds. Subsequently the average range ($\bar{x}$) was computed as the weighted arithmetic mean as shown in equation (7) after outlier removal (≥5σ).

$$\bar{x} = \frac{\sum_{i=1}^{N} f_i x_i}{\sum_{i=1}^{N} f_i} \quad (7)$$

In equation (7) x_i is an observation and f_i the frequency of that value. N is the total number of measurements which depends on the reading range of the individual sensor.

Precision is estimated as standard deviation (σ) of the measuring stack, and is computed using equation (8):

$$\sigma = \sqrt{\frac{\sum_{i=1}^{N} f_i \cdot (x_i - \bar{x})^2}{\sum_{i=1}^{N} f_i - 1}} \quad (8)$$

Maximum ranging capability is the maximum range from which the sensor can retrieve a measurement with a reasonable accuracy (i.e. 5% of the range).

Beam divergence is defined as the measure (in angular units) of the increment in beam diameter with distance from the optical aperture or antenna from which the sonic or electromagnetic beam emerges. A larger beam divergence leads to a larger ground footprint of the signal, which results in contamination of the signal if the surface is inhomogeneous. For the CLDS this parameter is negligible, since its ground footprint directly depends on the arm length A and the laser beam divergence is very low. Moreover, the CLDS provides images of each individual acquisition and the user can perform a-posteriori supervision to control if the

281 measured target is indeed the water surface. For the radar and the sonar, beam divergence is a
282 critical parameter to ensure that water is measured without interference from the surroundings.
283 This parameter has to be considered in order to monitor water bodies (e.g. large sinkholes, rivers
284 surrounded by dense vegetation), which only expose a narrow stretch of water to aerial view.
285 Indeed, because of loss of GNSS signal, flights under vegetation canopy or inside small cavities
286 (e.g. karst sinkholes) cannot be performed without losing position accuracy. Beam divergence
287 was estimated by acquiring measurements over water wells of small diameter, while water was
288 gradually being pumped out, as described in Appendix B.

289 ### *2.2.2. Airborne evaluation*

290 Numerous flights were conducted above a 0.02 km^2 lake located near Holte, Denmark
291 (55.821720°N, 12.509067°E). Water level in the lake is practically uniform. Whilst the sonar
292 and the CLDS identify only one target in the field of view, the radar can identify multiple targets
293 and reports the target angle for each of those. This requires an accurate identification of the
294 target, which is representative of the water surface. Indeed, sometimes multiple targets are
295 retrieved at nadir angle, for instance when vegetation is overhanging the water body. In that case,
296 postprocessing requires switching between different targets to obtain a result that is continuous
297 in time. Moreover, a low-pass digital filter was applied on the 15Hz raw radar data. A weighted
298 moving average (WMA) with a temporal window of 0.33 s (five observations) was applied to
299 smoothen the signal as shown in equation (9).

$$WMA_t = w_1 A_{t-2} + w_2 A_{t-1} + w_3 A_t + w_4 A_{t+1} + w_5 A_{t+2} \quad (9)$$

300

Weights (w1, w2…w5) are normally set to a high value for the measurement taken at the actual time (At) and to lower values for the previous and subsequent measurements.

.The overall accuracy of the system consisting of the GNSS receiver and the ranging sensor (σ_{tot}) is assumed to be that of two independent normally distributed variables: the ranging sensor accuracy and the GNSS accuracy (10).

$$\sigma_{tot} = \sqrt{\sigma_s^2 + \sigma_{RTK}^2} \qquad (10)$$

where σ_s is the accuracy of the ranging sensor and σ_{RTK} is the accuracy of the GNSS receiver.

3. Results

The first section of the results describes the technical performance of the ranging sensors when tested from a static position on the ground. Results are based on numerous tests conducted from bridges of different heights to compare the technical performance of the different sensors. The second section describes the results of the flight tests that are intended to evaluate the accuracy of the integrated system, i.e. GNSS receiver and sensors operating on board the UAV.

3.1. Ground-based performance results

Sensors demonstrated different performance in terms of accuracy and standard deviation of the measuring stack when tested from bridges of different heights. Appendix B lists the experimental settings for the static tests. Fig. 8 shows that the sonar usually tends to overestimate the range to water surface, which is probably caused by a slight penetration of the ultrasonic wave (42 kHz) below the water surface. Conversely, the radar usually tends to underestimate the range. The

authors guess that this is due to the post-processing of the raw data by the proprietary radar firmware.

Fig. 8

Table 1 summarizes the sensors' technical performance in terms of accuracy, standard deviation of the measurement stack, maximum ranging distance and beam divergence.

Table 1

Table 1 confirms that the sonar is the best sensor in terms of accuracy and standard deviation of the measurement stack. The CLDS has the lowest beam divergence. However, the radar is the sensor that combines the longest ranging capability, with accuracy and standard deviation that are only slightly worse than for the sonar. In Fig.9, two regression lines confirm the systematic error of radar and sonar. Plotted as function of the range, the regression line of the radar absolute error has a slope of -0.0090, while the slope of the sonar is 0.0083. After removal of this systematic error, the radar shows an accuracy of 0.5 % of the range, whilst the accuracy of the sonar is around 0.3%.

342 Fig.9

343

344

345 Finally, the accuracy of the retrieved vertical position has to be assessed. The accuracy of the
346 GNSS height depends mainly on: i) the integer ambiguity solution that has to be fixed to obtain
347 reliable observations, ii) the satellite geometry that affects the dilution of precision (DOP), iii)
348 multipath interference, especially because of signal reflection from the water surface.

349

350 *3.2. Airborne performance results*

351 In this section, we report the observations of two flights and we show a table summarizing the
352 entire dataset of flights over the lake. The range measured by each of the sensors and the altitude
353 retrieved by the GNSS are shown in Fig.10. The figure contains the entire dataset of observations
354 retrieved by the radar and sonar. Only not-a-number (NaN) values are removed. The sonar
355 outputs NaN when the range exceeds the maximum range capability (10 m). For the CLDS, we
356 only reported the measurements retrieved from images in which the laser dots are clearly
357 identifiable on the water surface.

358

359 Fig.10

360

361 Fig.10 shows an extremely high correlation (Pearson coefficient of 0.9991), between the GNSS
362 and the radar measurements, which indicates the consistency of our ranging technology. The
363 laser dots are generally distinguishable on the water surface only when the range to water surface
364 is less than 12-13 m . Similarly, the sonar provided accurate measurements only when the UAV

365 was hovering at low altitudes (less than 10 m from the water surface). Indeed, the radar and
366 sonar curves only overlap during these flight maneuvers.
367 In Fig. 11 we display the water level measured by the different sensors. Outliers (>2σ) were
368 removed.
369
370 Fig. 11
371
372 Mode value, mean and standard deviation of water level retrieved by each of the sensors are
373 reported in Table 2 under the column with flight date "04/04". The dispersion in water level
374 measurements retrieved by the system consisting of the radar and the GNSS receiver may be due
375 to multipath errors on the GNSS receiver. The cut-off angle for the elevation of the satellites,
376 which defines the angle below which GPS satellites are excluded, turned out to be a sensitive
377 parameter. The selected values for each flight are reported in Appendix B.
378 The water level values retrieved by the sonar had low accuracy, especially during high-speed
379 maneuvers. Since the range to water surface was greater than the maximum range capability of
380 the sonar for a significant portion of flight duration, the sonar retrieved many NaN values and
381 noisy observations. However, the mode value retrieved by the sonar is 24.14 m, which is close to
382 the mean value retrieved by the radar.
383 The CLDS exhibits only few observations due to limited range capability and low frame rate.
384 Moreover, natural light conditions complicate the recognition of the laser dots on the water
385 surface.
386 In order to estimate the absolute accuracy of the sensors, results were compared to in-situ
387 measurements of water level. For the in-situ measurement, an additional accurate RTK (Real

Time Kinematic) GNSS rover station was used, which was connected to a Danish GPS network. The position was averaged over a period of one minute which resulted in 24.10 m above the DVR90 geoid model (with an estimated accuracy of the GNSS rover station of around 5-6 cm). For this flight, the accuracy of the radar is thus better than 5 cm, the mode value of the sonar is around 4 cm from the ground truth, while the mean value retrieved by the CLDS is within two decimeters.

The second flight reported in Fig. 12 evaluated performance for higher drone altitude (up to 60 m) above the water surface.

Fig. 12

As shown in Fig. 12, the radar and the GNSS show very high correlation for the entire flight. The flight confirmed the limited ranging capability of the sonar (specified as 10 m, but already very noisy beyond 9 m). The CLDS retrieved ranges up to 13 m, however standard deviations increased significantly with range. In Fig. 13 we compare the water level retrieved by the three different sensors for this flight.

Fig. 13

Statistics of the flight are shown in Table 2 under the column “27/05”. In-situ water level was 24.01 m. Fig. 13 shows that the sonar measurements were unsuccessful. The CLDS, despite very high standard deviations, shows a mean value that is very close to the ground truth. The radar shows higher dispersion for long ranges. Moreover, systematic error is still observable, in fact

when the drone is at higher altitude, the retrieved water level increases by a few cm. System performance was confirmed in a number of other flights, as shown in Table 2 . Experimental settings, such as flight speed, illumination conditions, sensor settings for each flight, are explained in appendix B.

Table 2

Table 2 clearly indicates that the radar is the most reliable sensor, with the lowest standard deviation and good agreement with in-situ measurements. However, during some of the flights, the measured water level exhibits significant standard deviation also for the radar. This dispersion of the water level observations is caused not only by ranging errors but also by the GNSS. Indeed, during some flights, the geometrical configuration of GNSS satellites may have been suboptimal for accurate positioning. In addition to this, multipath of the GNSS signal may occur and degrade the accuracy of water level observations to ca. 7 cm.

The sonar provides very noisy measurements and exhibits a skewed distribution with a fat tail around 10 m, which is the maximum range of the sensor. While the mean value of water level does not provide an accurate estimate, the mode values measured by the sonar are very similar to the corresponding values measured by the radar.

For the CLDS, the mode value is not relevant because the number of observations is low. The CLDS standard deviation is quite large and in order to obtain accurate results the drone has to hover for several seconds.

4. Discussion

The ranging technology showed great potential in terms of accuracy, maximum range and beam divergence. In particular, the radar demonstrated the best performance in terms of accuracy and maximum range. The ranging sensor has to be integrated with carrier phase differential GNSS to retrieve water level. The accuracy of the integrated system consisting of GNSS receiver and radar is estimated to be better than 5-7 cm. This accuracy can be compared with the accuracy achievable with: i) airborne LIDARs, ii) spaceborne laser altimetry, iii) spaceborne radar altimetry and iv) ground-based stations as shown in Table *3*.

Table 3

Few studies report the accuracy of LIDAR system in measuring water surface, but it has been estimated to vary from few cm up to two tens of cm (Hopkinson et al., 2011). For airborne LIDAR systems, the inaccuracy of the onboard positioning systems has to be included. Similarly spaceborne laser altimetry from ICESat, which is the satellite altimeter with the smallest footprint (50–90 m) and the highest along-track resolution (40 Hz, 170 m), provides water surface elevation measurements for rivers with an accuracy at decimeter level. However the accuracy degrades in case of cloud cover (Phan et al., 2012). Additionally, simultaneous return from land and water are inevitable for small rivers and the identification of water surfaces remains problematic. The accuracy of radar altimetry sensors such as the systems on board

Jason-2 (Asadzadeh Jarihani et al., 2013), Envisat (Frappart et al., 2006) and Cryosat-2 (Song et al., 2015) is in the order of some tens of dm. Moreover, satellite radar altimetry generally has a spatial resolution lower than satellite laser altimetry and requires that rivers are hundreds of meters wide to avoid signal contamination by interfering land and vegetation (Maillard et al., 2015). With UAV-borne monitoring, water surface and interfering surroundings can be clearly separated due to the smaller ground footprint, and the possibility to retrieve individual radar target angles. However, for very narrow fields of view, the CLDS is the only sensor that can provide reliable water level measurements. Image analysis as part of the post-processing workflow ensures that measurement are accepted only if the monitored target is the water surface. This is the case for rivers surrounded by dense riparian vegetation or for small targets such as karst sinkholes, e.g. on the Yucatán Peninsula (Gondwe et al., 2010). Our CLDS solution overcomes the limitations of traditional red wavelength time-of-flight (TOF) laser distance meters, which are not suitable for ranging to water surfaces, because the reflectivity of water is very low for red visible wavelengths.

Only ground-based hydrometric stations ensure an accuracy higher than the one achieved with UAV-based monitoring, but coverage and reliability of in-situ monitoring networks have been degrading in many regions of the world. Moreover, despite providing high accuracy and temporal resolution, in-situ stations acquire only local measurements and tend to fail during extreme events. Therefore, UAV-based water level monitoring is beneficial for the monitoring of a wide range of hydrological systems, including small-scale rivers, ephemeral lakes, sinkholes, meltwater lakes, etc… UAV-based water level observations can resolve the spatial multidimensional variability of rivers. Indeed, UAVs can monitor water level along and across the river course, in order to obtain water slope and assess interaction between rivers and adjacent

floodplains. Improved sharpness and reliability of estimates of surface water-groundwater interaction using UAV-based monitoring of river water levels have already been reported (Bandini et al., 2016). Furthermore, UAVs can sense water level in unconventional remote sensing targets such as sinkholes or cenotes. This could potentially improve mapping of phreatic surfaces, for instance for the Yucatan peninsula (Bauer-Gottwein et al., 2011). Additionally, UAVs can potentially be used during extreme events when in-situ monitoring stations often fail and satellite observations do not ensure the required spatial and temporal resolution. Thus, UAVs have the potential to improve flood risk assessment. However, the ±7cm accuracy of our technology may still be insufficient for rivers flowing through low-lying terrain. Nonetheless, the accuracy is better than other spaceborne and airborne technologies and UAVs have a great potential in improving flood mapping because they allow optimal timing of the observations and high spatial resolution. UAV-based observations of water level in the flooded areas allow determination of stage-damage curves (Cammerer et al., 2013) which are essential for the design of insurance policies.

5. Conclusions

UAV-based remote sensing of river and lake water level (orthometric height) has the potential to fill the gap between in-situ measurements and spaceborne remote sensing. It ensures: i) high accuracy, ii) optimal spatial resolution, iii) flexible timing of the sampling, and iv) precise tracking of lakes and rivers. Different water surface ranging sensors were tested: a radar, a sonar, and a CLDS.

Static (on ground) and dynamic (airborne) tests demonstrated the following results:

- The radar showed the best accuracy and longest maximum range. Despite having a resolution of only 10 cm, averaging the 15 Hz primary data, an accuracy of 0.5% of the range can be achieved after correction of a negative bias of 0.9% of the range.
- The sonar provided unreliable results for high ranges or high speeds. Our results show that the sonar generally overestimates the range to water surface. However, when the UAV flies at a stable and low height, the accuracy is down to a few centimeters.
- The CLDS is less accurate than the radar. However, it has the lowest beam divergence and is useful when only a narrow field of view to the water surface is available for sensing.

Water level can be measured on board UAVs by subtracting the range to water surface from the vertical position retrieved by the GNSS receiver. Dynamic (airborne) tests have been performed on the positioning technology and the GNSS receiver had a vertical accuracy around 4-6 cm (2σ) and had an expected horizontal accuracy around 2 cm (2σ). However, multipath of the GNSS signal causes problems above water and the choice of the cut-off satellite elevation angle has a considerable influence on the position accuracy.

The integrated system GNSS receiver and radar is able to measure water level with an overall accuracy better than 5-7 cm when the UAV flies at a speed of few km/h.

Future research should include different types of sonar sensors, trading off signal penetration below the water surface (more penetration at lower frequencies) and interference of the propeller noise (more interference at higher frequencies). Moreover, research efforts are ongoing to develop new radars with higher measurement resolution, exploiting other region of the microwave spectrum commonly used in radar altimetry such as Ku and Ka bands.

The master thesis from Reyna Gutierrez, J. A. (2013) ''Monitoring and modeling of regional groundwater flow on the Yucatán Peninsula'' can be obtained from the authors upon request.

Acknowledgements

The Innovation Fund Denmark is acknowledged for providing funding for this study via the project Smart UAV [125-2013-5].

References

Alsdorf, D.E., Rodriguez, E., Lettenmaier, D.P., 2007. Measuring surface water from space. Rev. Geophys. 45, 1–24. doi:10.1029/2006RG000197.1

Anderson, K., Gaston, K.J., 2013. Lightweight unmanned aerial vehicles will revolutionize spatial ecology. Front. Ecol. Environ. 11, 138–146. doi:10.1890/120150

Asadzadeh Jarihani, A., Callow, J.N., Johansen, K., Gouweleeuw, B., 2013. Evaluation of multiple satellite altimetry data for studying inland water bodies and river floods. J. Hydrol. 505, 78–90. doi:10.1016/j.jhydrol.2013.09.010

Bandini, F., Butts, M., Vammen Torsten, J., Bauer-Gottwein, P., 2016. Water level observations from Unmanned Aerial Vehicles (UAVs) for improving probabilistic estimations of interaction between rivers and groundwater. Geophys. Res. Abstr. 18, EGU2016-3144.

Bauer-Gottwein, P., Gondwe, B.R.N., Charvet, G., Marin, L.E., Rebolledo-Vieyra, M., Merediz-Alonso, G., 2011. Review: The Yucatan Peninsula karst aquifer, Mexico. Hydrogeol. J. 19, 507–524. doi:10.1007/s10040-010-0699-5

Birkett, C.M., 1998. Contribution of the TOPEX NASA Radar Altimeter to the global monitoring of large rivers and wetlands. Water Resour. Res. 34, 1223. doi:10.1029/98WR00124

Birkett, C.M., Mertes, L. a K., Dunne, T., Costa, M.H., Jasinski, M.J., 2002. Surface water dynamics in the Amazon Basin: Application of satellite radar altimetry. J. Geophys. Res. Atmos. 107, LBA-26. doi:10.1029/2001JD000609

Calmant, S., Seyler, F., Cretaux, J.F., 2008. Monitoring continental surface waters by satellite altimetry. Surv. Geophys. 29, 247–269. doi:10.1007/s10712-008-9051-1

Cammerer, H., Thieken, A.H., Lammel, J., 2013. Adaptability and transferability of flood loss

552 functions in residential areas. Nat. Hazards Earth Syst. Sci. 13, 3063–3081.
553 doi:10.5194/nhess-13-3063-2013

554 Colomina, I., Molina, P., 2014. Unmanned aerial systems for photogrammetry and remote
555 sensing: A review. ISPRS J. Photogramm. Remote Sens. 92, 79–97.
556 doi:10.1016/j.isprsjprs.2014.02.013

557 Danko, T., 2004. Webcam Based DIY Laser Rangefinder [WWW Document]. URL
558 https://sites.google.com/site/todddanko/home/webcam_laser_ranger (accessed 11.9.15).

559 Detert, M., Weitbrecht, V., 2015. A low-cost airborne velocimetry system: proof of concept. J.
560 Hydraul. Res. 53, 532–539. doi:10.1080/00221686.2015.1054322

561 Featherstone, W.E., 2001. Absolute and relative testing of gravimetric geoid models using
562 Global Positioning System and orthometric height data. Comput. Geosci. 27, 807–814.
563 doi:10.1016/S0098-3004(00)00169-2

564 Frappart, F., Calmant, S., Cauhopé, M., Seyler, F., Cazenave, A., 2006. Preliminary results of
565 ENVISAT RA-2-derived water levels validation over the Amazon basin. Remote Sens.
566 Environ. 100, 252–264. doi:10.1016/j.rse.2005.10.027

567 Gondwe, B.R.N., Lerer, S., Stisen, S., Marín, L., Rebolledo-Vieyra, M., Merediz-Alonso, G.,
568 Bauer-Gottwein, P., 2010. Hydrogeology of the south-eastern Yucatan Peninsula: New
569 insights from water level measurements, geochemistry, geophysics and remote sensing. J.
570 Hydrol. 389, 1–17. doi:10.1016/j.jhydrol.2010.04.044

571 Hale, G.M., Querry, M.R., 1973. Optical Constants of Water in the 200-nm to 200-microm
572 Wavelength Region. Appl. Opt. 12, 555–563. doi:10.1364/AO.12.000555

573 Hopkinson, C., Crasto, N., Marsh, P., Forbes, D., Lesack, L., 2011. Investigating the spatial
574 distribution of water levels in the Mackenzie Delta using airborne LiDAR. Hydrol. Process.
575 25, 2995–3011. doi:10.1002/hyp.8167

576 Kiel, B., Alsdorf, D., LeFavour, G., 2006. Capability of SRTM C- and X-band DEM Data to
577 Measure Water Elevations in Ohio and the Amazon. Photogramm. Eng. Remote Sens. 72,
578 313–320. doi:10.14358/PERS.72.3.313

579 Kleinherenbrink, M., Ditmar, P.G., Lindenbergh, R.C., 2014. Retracking Cryosat data in the
580 SARIn mode and robust lake level extraction. Remote Sens. Environ. 152, 38–50.
581 doi:10.1016/j.rse.2014.05.014

582 Kleinherenbrink, M., Lindenbergh, R.C., Ditmar, P.G., 2015. Monitoring of lake level changes
583 on the Tibetan Plateau and Tian Shan by retracking Cryosat SARIn waveforms. J. Hydrol.
584 521, 119–131. doi:http://dx.doi.org/10.1016/j.jhydrol.2014.11.063

585 Lawford, R., Strauch, A., Toll, D., Fekete, B., Cripe, D., 2013. Earth observations for global
586 water security. Curr. Opin. Environ. Sustain. 5, 633–643. doi:10.1016/j.cosust.2013.11.009

587 Lee, H., Beighley, R.E., Alsdorf, D., Jung, H.C., Shum, C.K., Duan, J., Guo, J., Yamazaki, D.,
588 Andreadis, K., 2011. Characterization of terrestrial water dynamics in the Congo Basin
589 using GRACE and satellite radar altimetry. Remote Sens. Environ. 115, 3530–3538.
590 doi:10.1016/j.rse.2011.08.015

LeFavour, G., Alsdorf, D., 2005. Water slope and discharge in the Amazon River estimated using the shuttle radar topography mission digital elevation model. Geophys. Res. Lett. 32, L17404. doi:10.1029/2005GL023836

Lejot, J., Delacourt, C., Piégay, H., Fournier, T., Trémélo, M.-L., Allemand, P., 2007. Very high spatial resolution imagery for channel bathymetry and topography from an unmanned mapping controlled platform. Earth Surf. Process. Landforms 32, 1705–1725. doi:10.1002/esp.1595

Luo, C., Nightingale, J., Asemota, E., Grecos, C., 2015. A UAV-Cloud System for Disaster Sensing Applications, in: 2015 IEEE 81st Vehicular Technology Conference (VTC Spring). IEEE, pp. 1–5. doi:10.1109/VTCSpring.2015.7145656

Maillard, P., Bercher, N., Calmant, S., 2015. New processing approaches on the retrieval of water levels in Envisat and SARAL radar altimetry over rivers: A case study of the São Francisco River, Brazil. Remote Sens. Environ. 156, 226–241. doi:10.1016/j.rse.2014.09.027

Phan, V.H., Lindenbergh, R., Menenti, M., 2012. ICESat derived elevation changes of Tibetan lakes between 2003 and 2009. Int. J. Appl. Earth Obs. Geoinf. 17, 12–22. doi:10.1016/j.jag.2011.09.015

Reyna Gutierrez, J.A., 2013. Monitoring and modeling of regional groundwater flow on the Yucatán Peninsula. Unpubl. master's thesis, Tech. Univ. Denmark.

Rodriguez, E., Morris, C., Belz, J., 2006. An assessment of the SRTM topographic products. Photogramm. Eng. Remote Sensing 72, 249–260. doi:0099-1112/06/7203–0249/$3.00/0

Schumann, G., Matgen, P., Cutler, M.E.J., Black, a., Hoffmann, L., Pfister, L., 2008. Comparison of remotely sensed water stages from LiDAR, topographic contours and SRTM. ISPRS J. Photogramm. Remote Sens. 63, 283–296. doi:10.1016/j.isprsjprs.2007.09.004

Schutz, B.E., Zwally, H.J., Shuman, C. a., Hancock, D., DiMarzio, J.P., 2005. Overview of the ICESat mission. Geophys. Res. Lett. 32, 1–4. doi:10.1029/2005GL024009

Song, C., Ye, Q., Sheng, Y., Gong, T., 2015. Combined ICESat and CryoSat-2 altimetry for accessing water level dynamics of Tibetan lakes over 2003-2014. Water (Switzerland) 7, 4685–4700. doi:10.3390/w7094685

Tauro, F., Petroselli, A., Arcangeletti, E., 2015. Assessment of drone-based surface flow observations. Hydrol. Process. 30, 1114–1130. doi:10.1002/hyp.10698

Tauro, F., Porfiri, M., Grimaldi, S., 2016. Surface flow measurements from drones. J. Hydrol. 540, 240–245. doi:10.1016/j.jhydrol.2016.06.012

Villadsen, H., Andersen, O.B., Stenseng, L., Nielsen, K., Knudsen, P., 2015. CryoSat-2 altimetry for river level monitoring — Evaluation in the Ganges–Brahmaputra River basin. Remote Sens. Environ. 168, 80–89. doi:10.1016/j.rse.2015.05.025

Watts, A.C., Ambrosia, V.G., Hinkley, E.A., 2012. Unmanned Aircraft Systems in Remote Sensing and Scientific Research: Classification and Considerations of Use. Remote Sens. 4(6), 1671–1692. doi:10.3390/rs4061671

Wingham, D.J., Francis, C.R., Baker, S., Bouzinac, C., Brockley, D., Cullen, R., de Chateau-Thierry, P., Laxon, S.W., Mallow, U., Mavrocordatos, C., Phalippou, L., Ratier, G., Rey, L., Rostan, F., Viau, P., Wallis, D.W., 2006. CryoSat: A mission to determine the fluctuations in Earth's land and marine ice fields. Adv. Sp. Res. 37, 841–871. doi:10.1016/j.asr.2005.07.027

Yuen, H., Princen, J., Illingworth, J., Kittler, J., 1990. Comparative study of Hough Transform methods for circle finding. Image Vis. Comput. 8, 71–77. doi:10.1016/0262-8856(90)90059-E

Zhang, G., Xie, H., 2010. Water level changes of two Tibetan lakes Nam Co and Selin Co from ICESat altimetry data, in: 2010 Second IITA International Conference on Geoscience and Remote Sensing. IEEE, pp. 463–466. doi:10.1109/IITA-GRS.2010.5602644

Appendix A. Calibration of the CLDS

The CLDS needs to be calibrated in order to provide a ranging measurement. Calibration has been performed acquiring multiple range measurements (from 0 to 12 m) using a black vertical wall as calibration target. Since the focal length of the camera is not exactly known, equation (4) must be used and the calibration is used to retrieve the coefficients r_{pp1} and r_0 for converting from pixel units to angular units. The relationships between θ' and the distance from the laser dots to the center of the image (PFC) are shown in Fig. A.1 for each of the laser pointers. Alternatively, Fig. A.2 depicts the relationship between the range to the target and PFC.

Fig. A.1 Fig. A.2

Fig. A.1 and Fig. A.2 show that the laser pointers' curves are not coincident as a consequence of the slight asymmetry of the layout (imaging sensor of the camera not placed exactly in the middle of the two laser pointers). As confirmed by Fig. A.1, the relationship between PFC and the measured angle is approximately linear for each of the two laser pointers. Calibration has shown an r (Pearson linear correlation coefficient of determination) of 0.99978 and an RMSE (Root Mean Square Error) of 7.16 cm for the blue laser (left laser); an r of 0.99937 and an RMSE of 8.29 cm for the green laser (right laser). Calibration error is displayed in Fig. A.3.

Fig. A.3

Fig. A.4

Fig. A.*3* demonstrates that the advantage of using two laser pointers is improved error assessment. Considering the average of the measurements of the two laser pointers, calibration

RMSE is reduced to 5.61 cm. When range to water surface has to be retrieved, the precise computation of PFC is more problematic than during the simple calibration procedure. Indeed, while laser dots can be normally identified as in Fig. A.4 (a), laser dots on the water surface might have contours that are less defined as in Fig. A.4 (b). Sometimes even multiple laser dots are visible, as shown in Fig. A.4 (c). This is caused by: i) atmospheric scattering processes, ii) scattering processes due to water waviness iii) vibrations of the UAV. The laser light reflected from the bottom is occasionally visible in the image, especially in case of shallow or very clear water, as shown in Fig. A.4 (d). Experiments showed that the uncertainty in the PFC increases with the range to water surface. This is displayed in Fig. A.5 with the curve PFC-σ_{PFC}. Fig. A.5 clearly shows that the green laser exhibits larger uncertainty than the blue laser since green wavelengths are scattered to a greater extent than blue wavelengths. The expected uncertainty in the range can be estimated using the derivative of the range function as shown in equation (A.1).

$$\sigma(range) = \frac{\partial range}{\partial(PFC)}\sigma(PFC) \tag{A.1}$$

Fig. A.5 Fig. A.6

Fig. A.6 shows that the uncertainty of the range estimate increases with the range to water surface. This is a consequence of: i) the derivative of the curve in Fig. A.2 that increases in absolute value for longer ranges (small inaccuracy in PFC determines high imprecision in the range observation). The derivative is lower in absolute terms for the blue laser, because of the prototype layout. ii) Increasing uncertainty of the PFC with increasing range (i.e. decreasing PFC).

Appendix B. Experimental settings

In Table B.1 we report the location, the date and time of the day, the environmental conditions and the water flow speed for each of the static tests. The mean value and the standard deviation of the measurements are shown in Figure 8.

Here Table B.1

Illumination conditions are reported in the table because they affect visibility of the laser dots on the water surface. This factor has been critical only in case of sun glint conditions during which laser dots are hardly identifiable. On the other hand, wind stress and current can affect water surface roughness and change the intensity of the backscattered radar signal.

Estimates of beam divergence for the different sensors were obtained from tests above a cylindrical water well of diameter (D) equal to 0.7 m. The sensors were placed exactly in the middle of the water well as shown in Fig. B.1. The initial range between the sensors and the water surface was 0.5 m. Subsequently, the well was pumped to gradually increase the range to the water surface. Beam divergence (φ) was then computed according to equation B.1.

$$\varphi = 2 * \tan^{-1} \frac{D}{2 \cdot r_c} \qquad (B.1)$$

In equation B.1, r_c is the critical range i.e. the range at which the sensor first produced erroneous results because of interference with the well walls. Fig. B.1 provides an illustration of the experimental setup.

Fig. B.1

While the CLDS was able to retrieve the range to water surface for all water levels (beam width is constant and equal to the arm length), the beam divergences of the radar and the sonar were estimated using this method. For the radar, interferences started to occur at a range of 1.3 m, and for the sonar at 1 m. Equation B.1, then gives beam divergence of the radar as ca. 30° and beam divergence for the sonar as ca. 40°.

Table B.2 shows the flight records for the tests conducted over the lake to estimate the airborne accuracy of the system.

Table B.2

As Table B.2 shows, the GNSS satellite cut-off angle settings are different between the flights. The cut-off angle showed an influence on the position accuracy, and thus on the water level measurements, up to 1-2 cm. Larger cut-off angles reduce the number of satellites in the field of view of the GNSS antenna, while smaller cut-off angles might increase multi-path effects (e.g. GNSS signal reflected by the water surface).

Average and vertical speed was varied between the different flights to test the synchronization between the GNSS system and the different sensors. Indeed, since water level is constant in the lake, when the drone rapidly changes its altitude, equivalent variations should be recorded by the ranging sensors and the GNSS system. Synchronization between the radar, sonar and the GNSS was obtained at the 30 ms level, while synchronization with the CLDS was obtained at the 0.2 s

level. The synchronization between the GNSS system and the CLDS is slightly worse because, even though the SBC registers the time at which the camera is triggered, the actual time that the CMOS camera needs to take a picture is unknown.

Figures

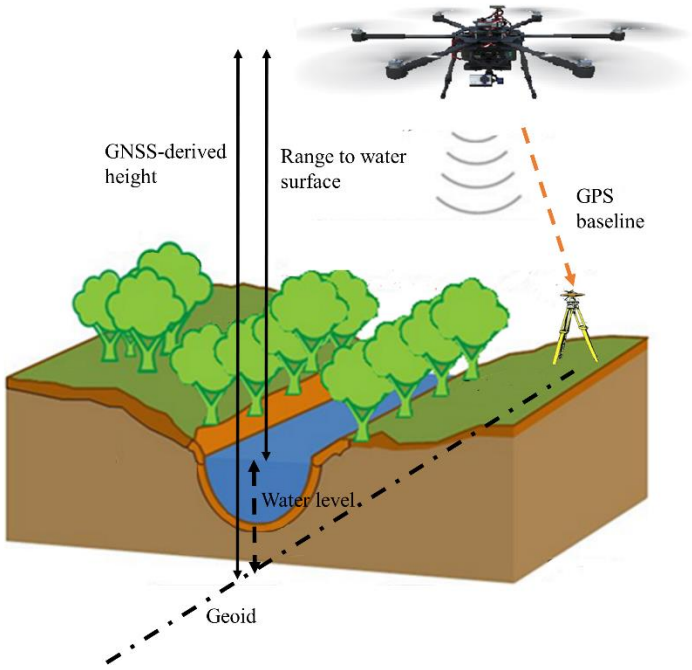

Fig. 1. Illustration of measurement principle for retrieving water level. The system includes: i) the UAV, ii) the sensors to measure the range from the UAV to the water surface, iii) a GNSS receiver on board the UAV providing accurate vertical and horizontal position. Centimeter-level position accuracy is obtained through the installation of an in-situ GNSS master station providing corrections for a kinematic post-processed solution.

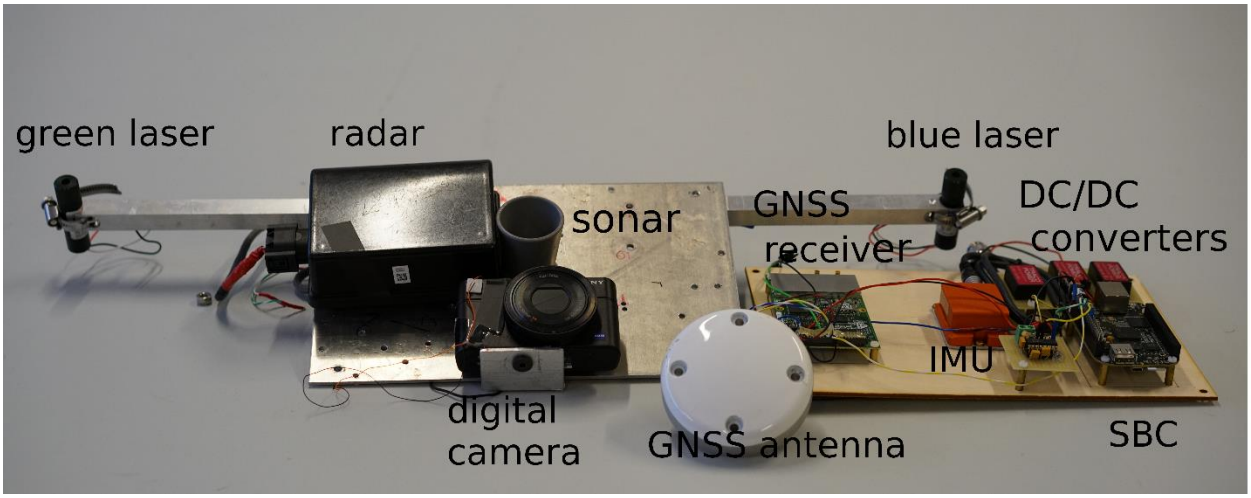

Fig. 2. Picture of the drone payload. It includes the three tested sensors (CLDS, radar and sonar), the GNSS system (antenna and receiver), the IMU, the Single Board Computer (SBC) and the power convertion units (DC/DC converters).

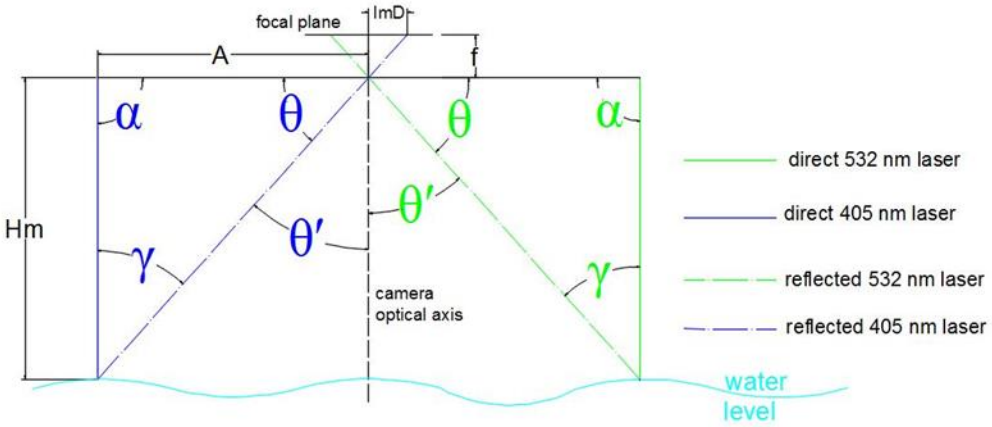

Fig. 3. Geometric configuration of the CLDS solution. A is the distance between the center of the camera and each of the laser pointers. α is the angle between each of the lasers and the focal plane of the camera. Hm is the distance between the camera and the water surface. ImD is the distance between the center of the image focal plane and each of the recorded laser light dots. f is the focal length of the camera. θ′ is the reflection angle. θ is its angle between the axis of the CLDS and the reflected ray. γ is the angle between incident and reflected ray. If α is 90° (as in the figure), γ is equal to θ′.

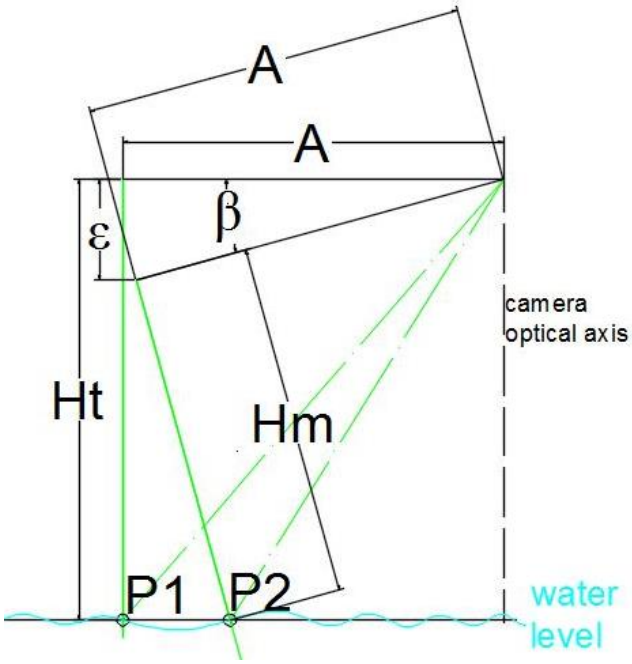

Fig. 4. Tilting angle: β is the angle between the horizontal line and the plane where the lasers and the camera are located.

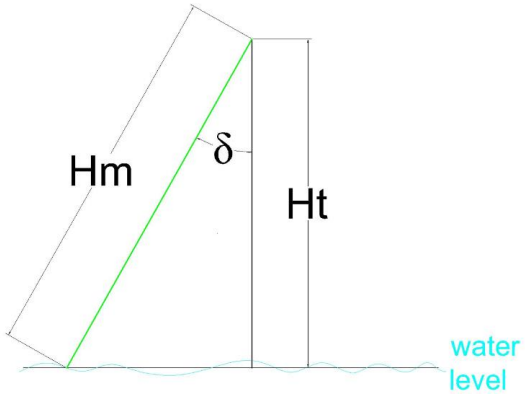

Fig. 5. Rotation angle: δ is the angle between the vertical line and optical axis of the camera.

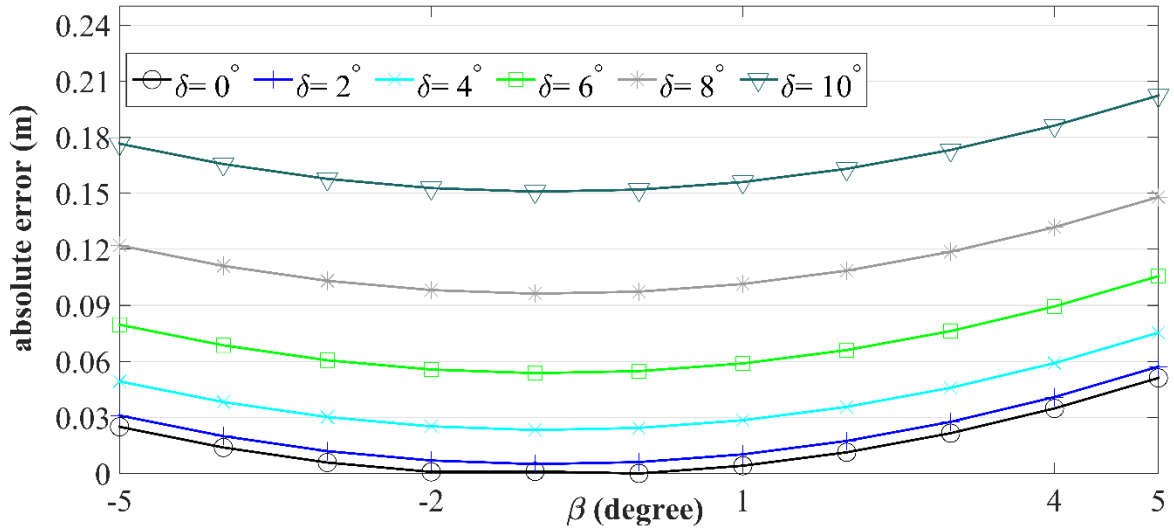

Fig. 6. Error as a function of displacement angles. Absolute error is shown for different tilting (β) and rotation (δ) angles at 10 m range.

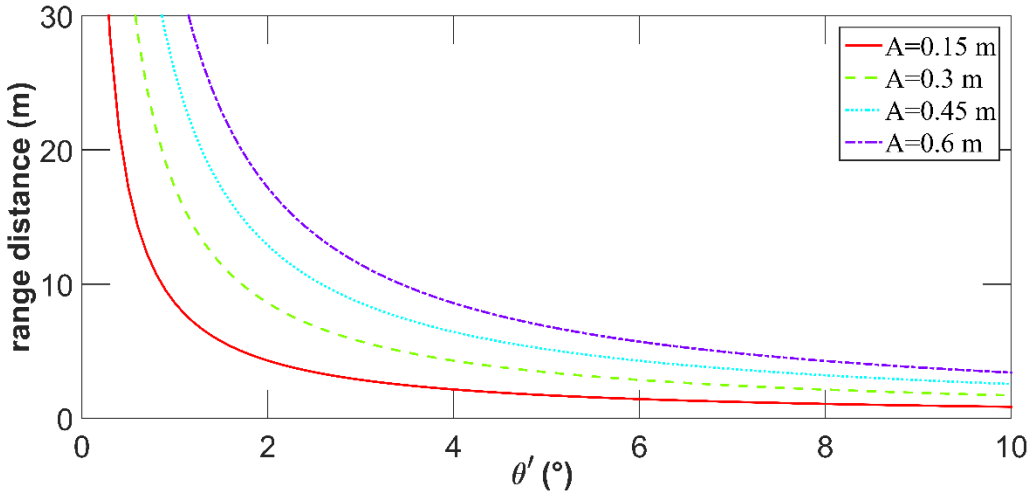

Fig. 7. Range distance as a function of the θ′ angle. The range function depends on the different length values of A, which is the distance between the laser source and the camera.

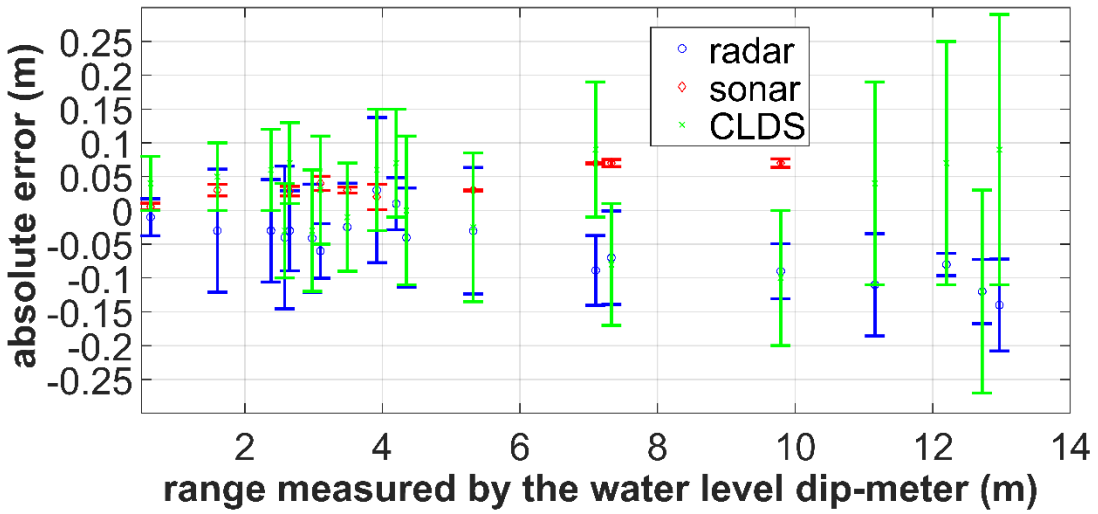

Fig. 8. Absolute error as a function of the range measured by each of the ranging sensors. Absolute error is computed using the water level dip meter as reference. The marker is the average error (bias) of all measurements taken for a specific range, while the bar shows the standard deviation.

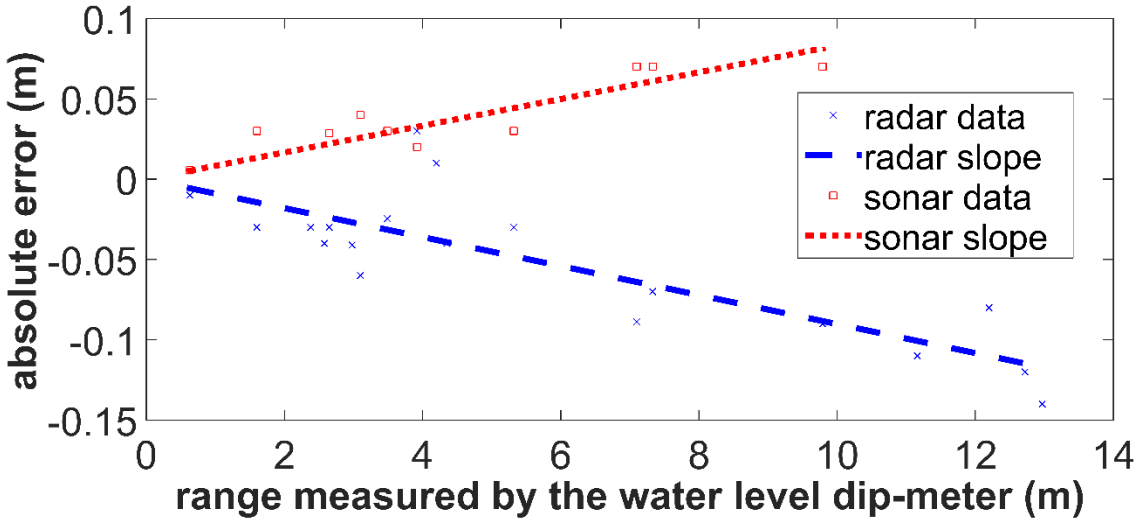

Fig. 9. Sonar and radar errors as a function of the range. Dots represent the measurements acquired by the radar and the sonar. The regression line shows that the absolute error is a function of the range.

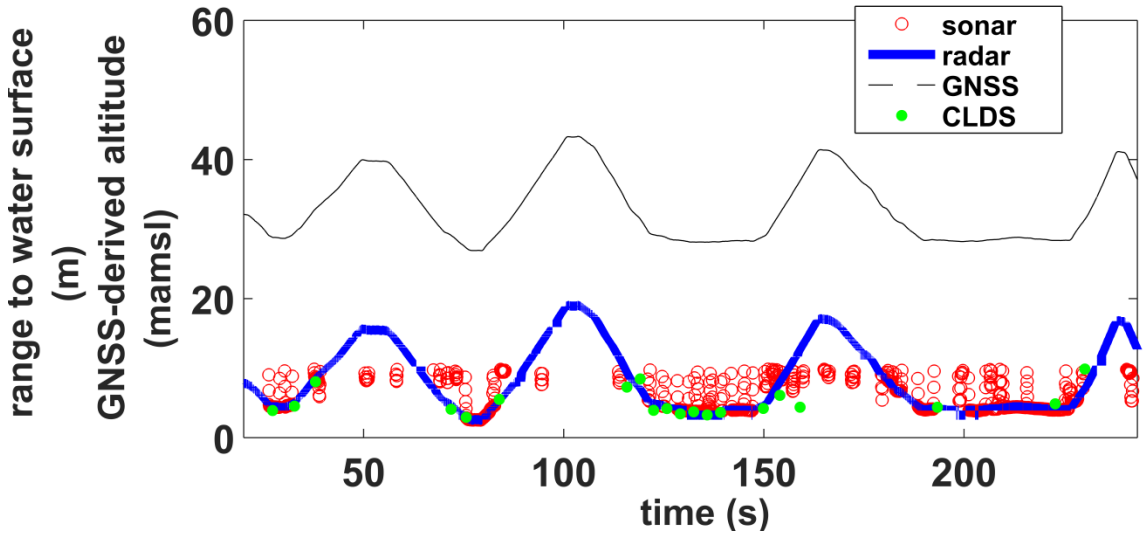

Fig. 10. Observations retrieved during the flight on April 4, 2016. The plot shows the range measured by the radar (blue), sonar (red), CLDS (green) in meter (m) to the water surface, and the drone altitude retrieved by the GNSS (black) in meter above mean sea level (mamsl).

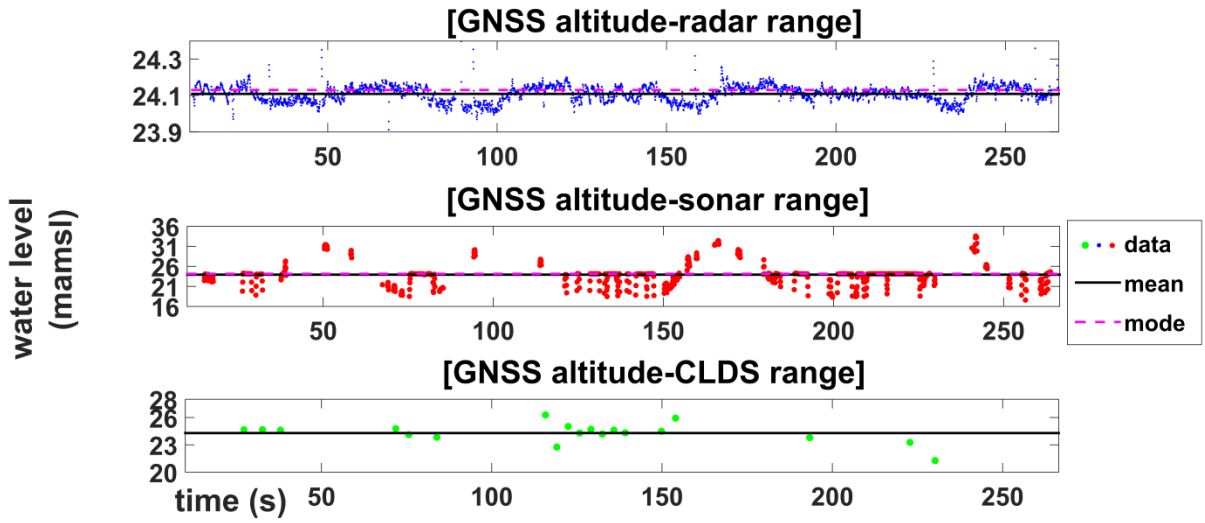

Fig. 11. Water level (mamsl) observations retrieved during the flight on April 4, 2016. Each of plots shows the water level observations measured by subtracting the range retrieved by each of the sensors (radar, sonar, CLDS) from the GNSS altitude. In each plot, the black line is the mean of the water level observations and the magenta line is the mode of those observations.

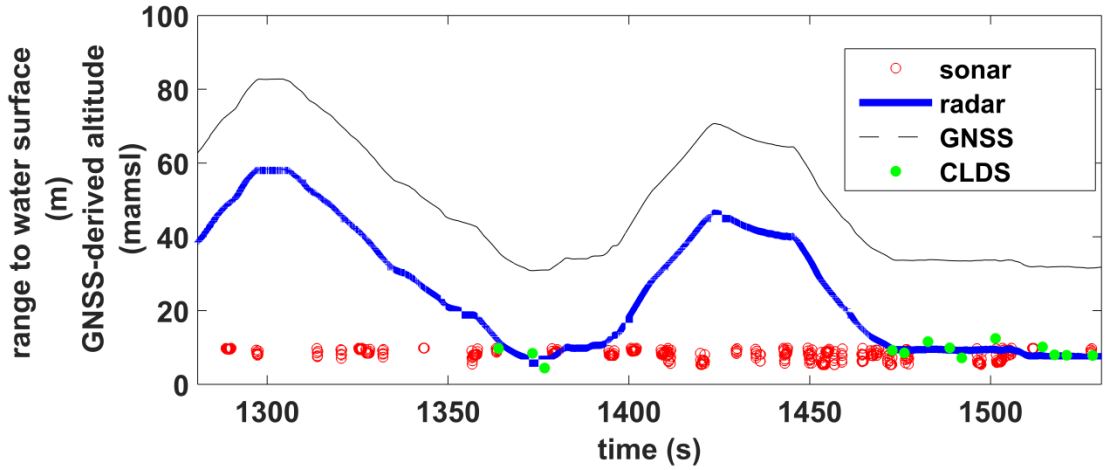

Fig. 12. Observations retrieved during the flight on May 27, 2016. The plot shows the range measured by the radar (blue), sonar (red), CLDS (green) in meter (m) to the water surface, and the drone altitude retrieved by the GNSS (black) in meter above mean sea level (mamsl).

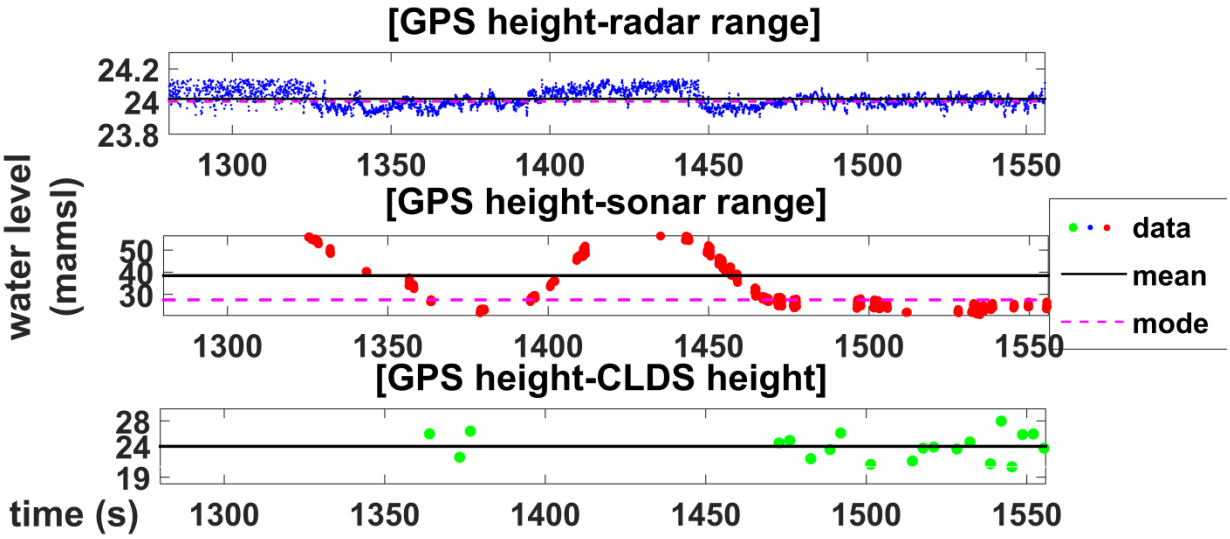

Fig. 13. Water level (mamsl) observations retrieved during the flight on May 27, 2016. Each of plots shows the water level observations measured by subtracting the range retrieved by each of the sensors (radar, sonar, CLDS) from the GNSS-derived altitude. In each plot, the black line is the mean of the water level observations and the magenta line is the mode of those observations.

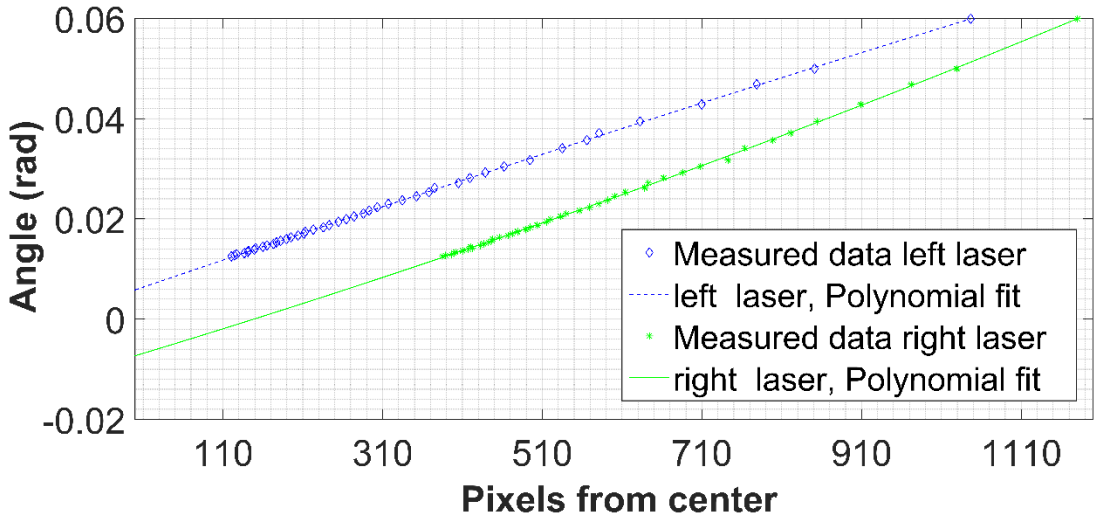

826
827
828 Fig. A.1. Relationship between the measuring angle θ′ and PFC.
829

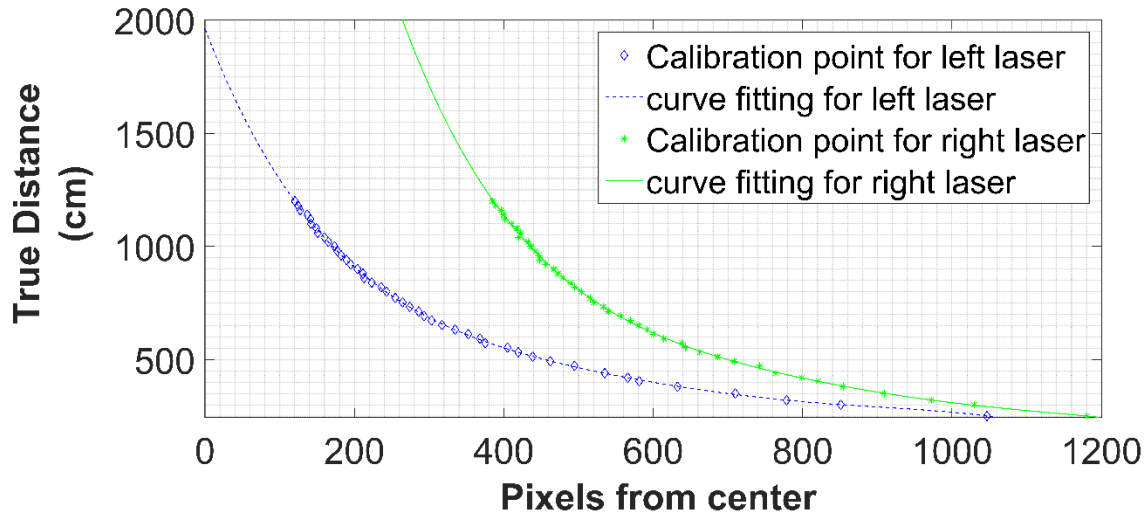

830
831
832
833 Fig. A.2. Relationship between the range to the target and PFC.
834
835
836
837

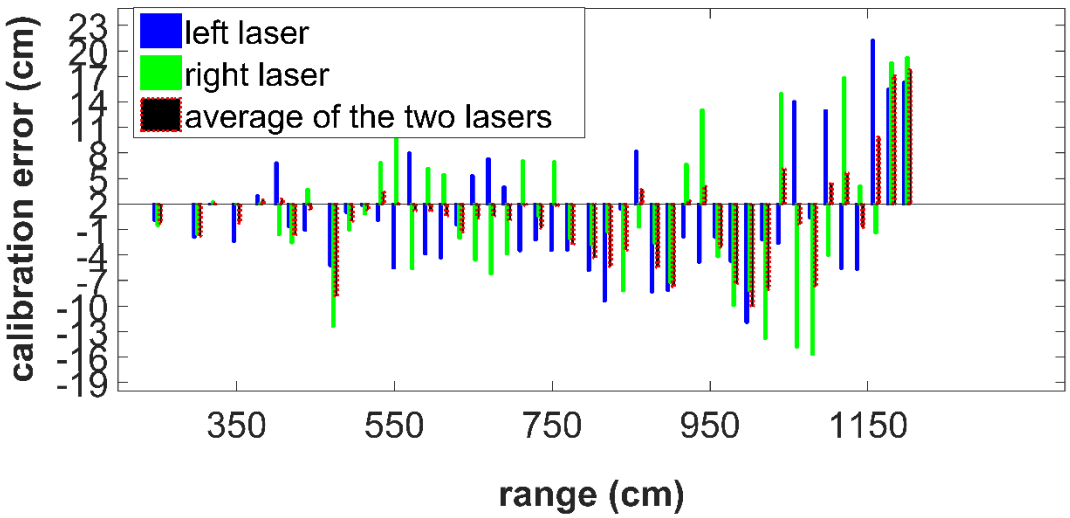

Fig. A.3. Calibration error for left laser (blue column), right laser (green column) and for the average (red column) between the two laser pointers.

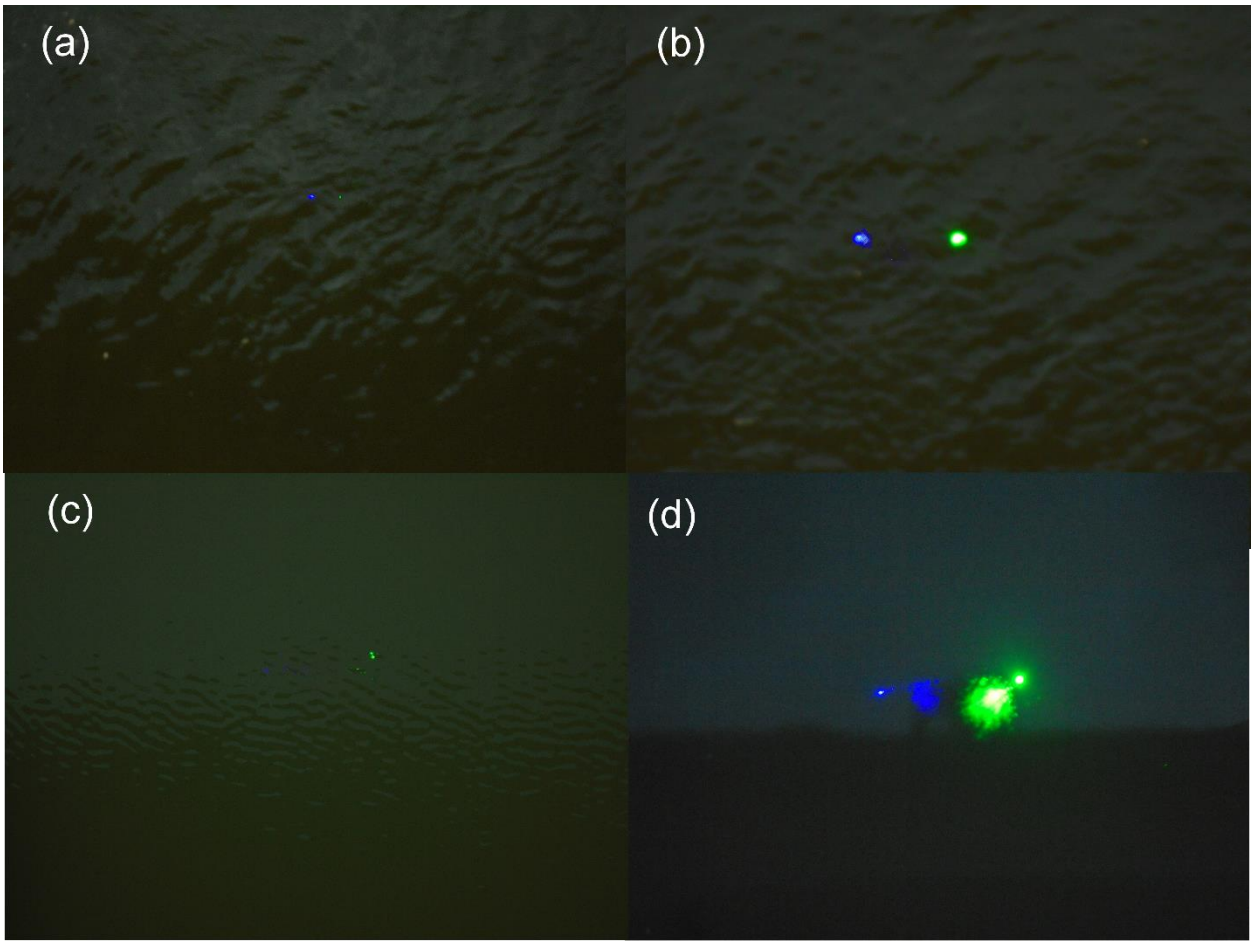

844

845 Fig. A.4. Airborne image of water surface taken by the CLDS. (a) the two laser dots are clearly identifiable (b)
846 larger laser dots with contours that are less identifiable (c) multiple green laser dots caused by multiple reflection
847 and scattering processes (d) laser light is reflected by the bottom (larger dots) and by the surface (smaller dots)

848

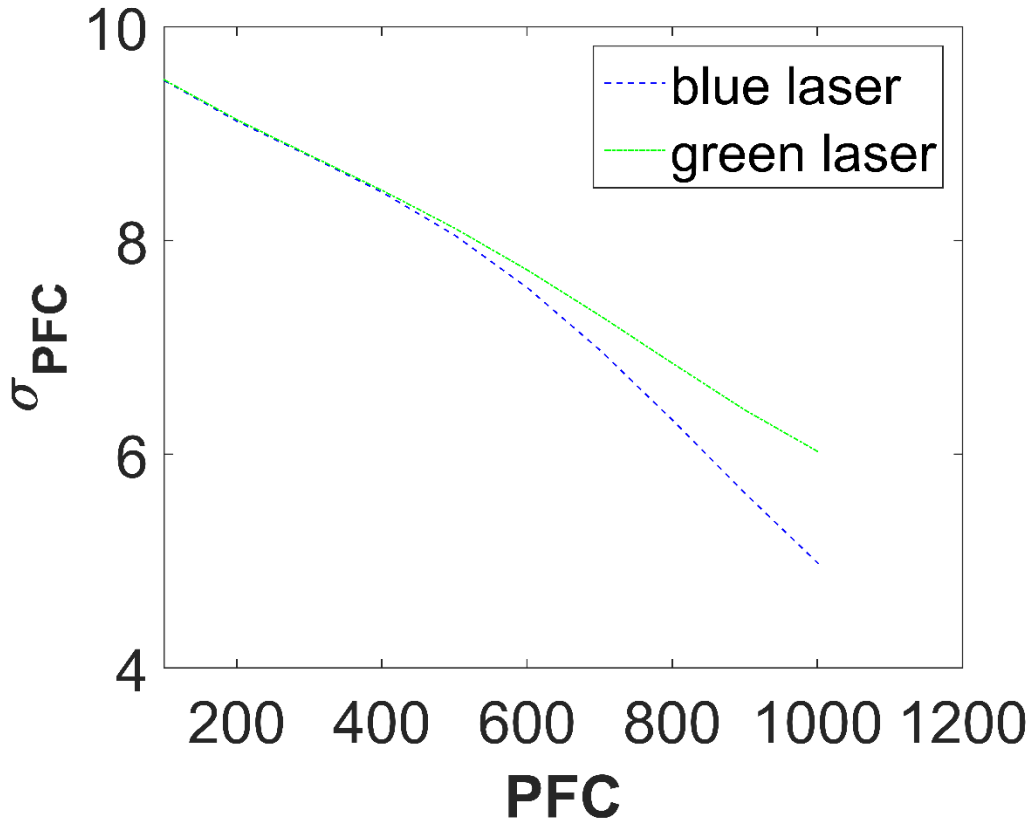

Fig. A.5. Uncertainty (σ_{PFC}) in computing the number of pixels as a function of PFC, for green and blue laser.

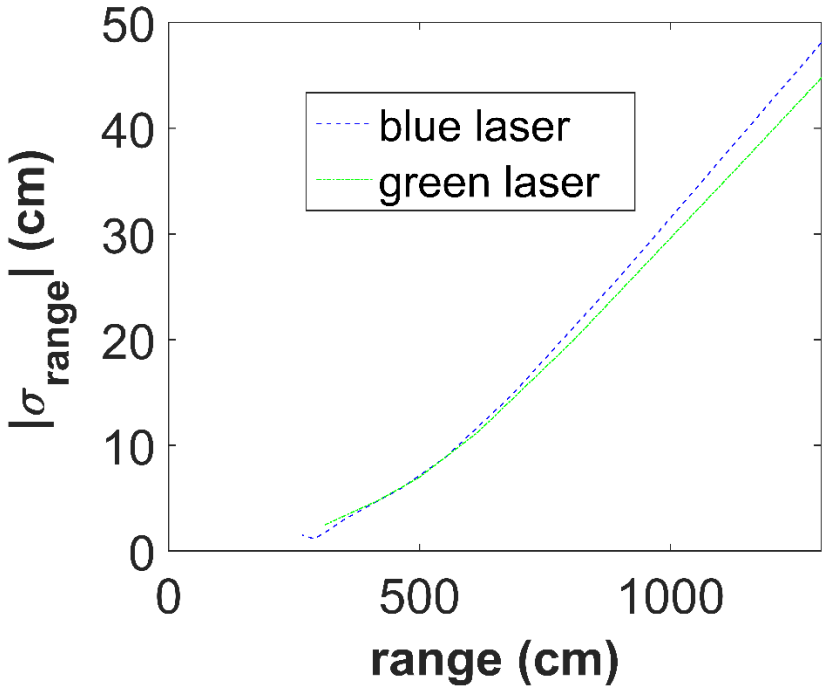

Fig. A.6. Absolute uncertainty in range measurement ($|\sigma_{range}|$) as a function of the range to the target, for green and blue laser.

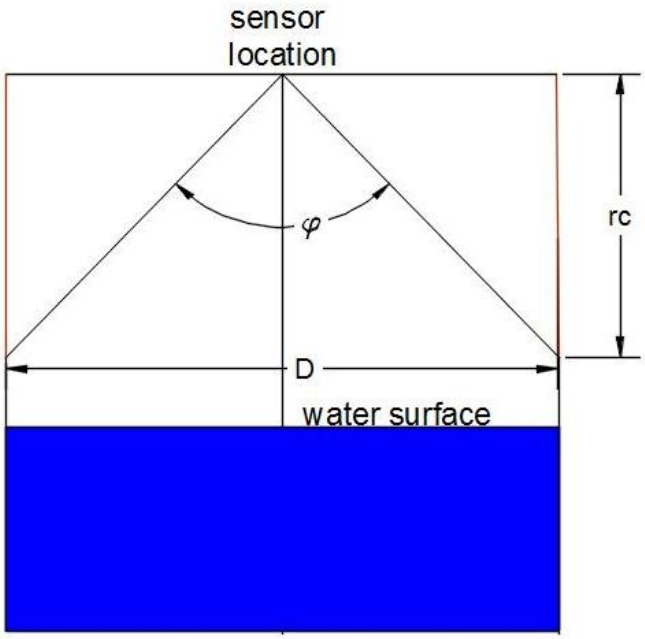

Fig. B.1. Schematic representation of the test conducted over the water well to retrieve beam divergence (φ) for each of the sensors. D is the diameter of the water well, r_c is the critical range.

Tables

Table 1. Technical performance of the sensors and of the GNSS receiver when tested in static mode.

	mean absolute error (percentage of the range)	**standard deviation of the stack**	**Maximum ranging distance**	**Beam divergence**
Radar	-1.09%	0.064 m	60 m near field 200 m far field	~30˚
Sonar	0.98%	0.007 m	10 m	>40˚
CLDS	1.5%	2.3 % of the range	13 m	negligible
GNSS receiver	negligible	Vertical	------	------

coordinates : 4-6

cm at 2 sigma

Table 2. Summary of the test flights over the lake. Each flight is named with the date (corresponding year is 2016). Ground truth was measured with a RTK GNSS rover station connected to the network of reference stations. Statistics concern the water level observations measured by subtracting the GNSS flight altitude from the range to water surface measured by each of the sensors. Statistics are computed after removal of the observations that lie beyond 2σ.

		Flight date (dd/mm/2016)				
Flight statistics		**17/03**	**04/04**	**13/04**	**05/13**	**27/05**
Ground truth (mamsl)		missing	24.10±0.06	24.13±0.06	24.04±0.06	24.01±0.06
Mean value (mamsl) of water level retrieved by	radar	24.10	24.11	24.20	24.11	24.02
	sonar	23.50	23.93	20.01	27.05	38.45
	CLDS	missing	24.29	24.81	24.82	23.93
Mode value (mamsl) of water level retrieved by	radar	24.18	24.13	24.10	24.12	24.00
	sonar	24.40	24.14	24.08	24.65	27.50
	CLDS	missing	21.27	24.56	24.41	20.66
Standard Deviation (m) in water level retrieved by	radar	0.07	0.05	0.08	0.09	0.05
	sonar	0.80	2.31	1.3	0.36	14.42
	CLDS	missing	1.08	0.95	1.68	2.05

Table 3. Accuracy and ground footprint of different techniques for observing water level

Location	Technique	Footprint	Accuracy	Reference
Airborne	LIDARs	20 cm-1 m	4-22 cm	(Hopkinson et al., 2011)
Spaceborne	laser altimetry (e.g. ICESat)	50–90 m	10 cm	(Phan et al., 2012)
Spaceborne	radar altimetry (e.g. ERS2, Envisat, Topex/Poseidon)	400 m-2 km	30-60 cm	(Frappart et al., 2006)
Ground-based	radar/sonar/pressure transducers	negligible	1 mm-10 cm	Widely known metrology
UAV-borne	radar altimetry	negligible	5-7 cm	Methodology described in this paper

Table B.1. Locations, settings and environmental conditions during static (on ground) tests. Coordinates are in WGS84. Country is either Denmark (DK) or Italy (IT). Range (m) is the value measured by the water level dip meter. Water speed has qualitatively been classified into no speed (still water), low (less than 0.4 m/s), medium (between 0.4 and 1 m/s), and high speed (more than 1 m/s). Wind speed has been qualitatively classified into no wind, low (wind less than 2 m/s), medium (between 2 m/s and 8 m/s), and high wind speed (more than 8 m/s). Illumination has been qualitatively classified into artificial lightening, low (less than 20 000 lux), medium (between 20 000 and 50 000 lux), and high illumination (more than 50 000 lux)

Latitude	Longitude	River	Country	Range to water	Date (dd/mm/2015)	Time of the day (hh:mm)	Flow speed	Wind	Illumination
55.783431	12.515610	Laboratory	DK	0.63	2/11	11:20	no	no	artificial
55.775211	12.470266	Mølleåen	DK	1.60	20/11	13:30	low	medium	low
55.775211	12.470266	Mølleåen	DK	2.38	20/11	11:41	low	medium	low
55.775211	12.470266	Mølleåen	DK	2.58	20/11	11:52	low	medium	low
55.775211	12.470266	Mølleåen	DK	2.65	10/10	11:20	low	high	low
55.775211	12.470266	Mølleåen	DK	2.98	1/10	14:10	low	medium	low
55.775211	12.470266	Mølleåen	DK	3.10	10/10	11:25	low	high	low
55.775211	12.470266	Mølleåen	DK	3.49	10/10	11:49	low	high	low
44.909645	10.991254	Sabbioncello	IT	3.92	22/12	16:00	low	low	low
55.775211	12.470266	Mølleåen	DK	4.20	10/10	14:10	low	high	medium
55.775211	12.470266	Mølleåen	DK	4.35	1/10	14:33	low	medium	low
45.038994	10.965141	Canale Bonifica	IT	5.32	22/12	13:00	low	low	medium

		Parmigiana,							
45.029723	10.959166	Canale della Bonifica Reggiana Montovana	IT	7.10	22/12	14:05	low	low	low
45.029726	10.960432	Canale della Bonifica Parmigiana	IT	7.33	22/12	9:30	low	low	low
44.650573	10.794755	Secchia	IT	9.79	29/10	12:00	medium	medium	medium
44.821261	10.994579	Secchia	IT	11.16	29/10	12:50	medium	medium	high
44.67578	10.860146	Secchia	IT	12.20	29/10	13:50	medium	medium	medium
45.008365	10.977453	Secchia	IT	12.72	29/10	20:30	medium	medium	low
44.727259	11.045292	Panaro	IT	12.97	29/10	8:30	medium	low	low

Table B.2. Summary of the test flights over the lake.

	Flight date (dd/mm/2016)				
Flight statistics	**17/03**	**04/04**	**13/04**	**05/13**	**27/05**
Take-off time (hh:mm)	15:00	12:20	13:20	13:00	12:00
Flight time over water (s)	500	270	200	250	260
Minimum-Maximum flight height (meter above water surface)	3-28	4-18.5	5-60	8-48	9-58
Average horizontal speed (m/s)	2	3	4	1	2
Average vertical speed (m/s)	0.1	1.1	1	0.3	0.3
Maximum vertical speed (m/s)	1	2	3	1.5	1
GPS cut-off angle (degree)	10	13	14	15	15